THE ASTROPHYSICAL JOURNAL, 517:866–882, 1999 June 1

A MULTIWAVELENGTH CAMPAIGN ON γ CASSIOPEIAE. III. THE CASE FOR MAGNETICALLY CONTROLLED CIRCUMSTELLAR KINEMATICS

MYRON A. SMITH[1] AND RICHARD D. ROBINSON[2]
Received 1998 August 7; accepted 1999 January 5

ABSTRACT

In two previous papers, we have discussed simultaneous *Rossi X-Ray Timing Explorer* (*RXTE*) and *Hubble Space Telescope* GHRS observations made of γ Cas (B0.5e) over a full day on 1996 March 14–15. The light curves generated from these data show features that anticorrelate and led us to conclude that the star has multiple surface activity centers that rotate into view every rotational cycle of 1.123 days. In a second paper we found that dips in the UV continuum (UVC) light curve are probably caused by the passage of cool, co-orbiting clouds that are suspended above surface X-ray–active centers. In this paper we use difference spectra from our >21 hr GHRS time series to investigate $\leq 2\%$ spectral variations within the photospheric Si IV 1394–1403 Å lines as well as smaller variations from features in neighboring wavelengths at 1382–1386 and 1404–1417 Å. Several difficulties arise in interpreting these variations as signatures of surface inhomogeneities, so we have studied both types of variations in the context of the kinematics of occulting circumstellar (CS) structures. By means of model-atmospheres codes and up-to-date line lists, we computed a grid of cloud opacity for various temperatures in our spectral range. Using these synthetic spectra, we are able to identify features as optically thick absorptions due to Fe II, Cr II, and C I lines from "cool" ($T < 10{,}000$ K) plasma, of Si IV, Si III, S IV, and Ni II lines from "warm" plasma ($\sim 10{,}000$–$18{,}000$ K), and of Si IV and Fe V lines from hot plasma ($\geq 30{,}000$ K). The variations of the cool- and hot-plasma lines are in phase with the UVC light curve while the warm-plasma line curves lead these curves by 3–4 hr. The cool- and warm-plasma lines participate in the blue-to-red deceleration and appear to be analogues of the "migrating subfeature" pattern found in optical lines by previous observers. The velocity range for these lines is consistent with limits of $\pm V \sin i$, suggesting that they are formed in corotating cloudlets that are distinct from the cool clouds we studied in a previous paper. In contrast, warm and hot-plasma lines are "ultrasharp features" ("USFs") that maintain a constant velocity for several hours. The USFs are visible over a wide velocity range, in some cases having a velocity of at least $+1500$ km s^{-1}. Both cooling and heating of circumstellar plasma is consistent with the existence of strong nonradiative processes operating in some regions above γ Cas. Additionally, the migrating subfeatures find a ready explanation in circumstellar cloudlets forced by magnetic forces into corotation, as was also inferred from the UVC light curve in Smith, Robinson, & Hatzes. The existence of the stationary ultrasharp absorption features, particularly at large positive velocities, is difficult to explain unless one invokes interactions between magnetic loops from the star and a putative field in the circumstellar disc. This picture holds the potential of explaining the hot, flaring character of this star's X-rays and predicts the existence of other X-ray–emitting γ Cas analogues as magnetic Be stars having dense CS discs.

Subject headings: circumstellar matter — stars: activity — stars: emission-line, Be — stars: individual (γ Cassiopeiae) — stars: rotation

1. INTRODUCTION

Discovered as a prototypical example of a Be star over 130 years ago, γ Casseiopeia (B0.5e) has become famous as one of the most panchromatically active stars on the H-R diagram. The production, maintenance, and dissipation of its circumstellar, equatorial disc has been documented through its Hα emission for nearly a full century (see, e.g., Doazan 1982; Horaguchi et al. 1994). One conspicuously peculiar facet of γ Cas's nature became apparent with the discovery that it is a prodigious emitter of X-rays (Jernigan 1976; Mason, White, & Sanford 1976). Its X-ray flux is at least several times that of other presumed nonbinary OB stars but is still some 20 times lower than the weakest X-ray–emitting member of the subgroup of Be X-ray binaries (BeXRBs). The star's unusual X-ray characteristics were accentuated by the report by Murakami et al. (1986) that its X-ray spectrum is consistent with a $\sim 10^8$ K plasma temperature. Moreover, these authors found that its X-ray light curve is punctuated by a continual pattern of both minor and major "flares" lasting a few minutes or less. In the optical region, the discovery of "migrating subfeatures" in Si III, He I, and lines of other ions by Yang, Ninkov, & Walker (1988), Horaguchi et al. (1994), and Smith (1995) have made this object a prototype of a new group of Be stars (see, e.g., Balona 1999).

Unlike the star itself, the circumstellar environment of γ Cas at first appears to offer few novelties. Studies of the resonance lines of Si IV, C IV, and N V formed in this star's wind have indicated the presence of discrete absorption features (DACs) and resulted in an estimated (and unnoteworthy) mass-loss rate of $5 \times 10^{-8}\ M_\odot\ \mathrm{yr}^{-1}$ (Stee et al. 1995). It was also discovered that the V/R emission

[1] STScI/CSC, Space Telescope Science Institute, 3700 San Martin Drive, Baltimore, MD 21218; msmith@stsci.edu.
[2] Catholic University of America, and LASP, Goddard Space Flight Center.

ratios of the Balmer lines and the column densities of the UV resonances lines vary cyclically with time (see, e.g., Doazan et al. 1987; Telting & Kaper 1994). Such variations, as well as V/R variations from the discs of other Be stars, appear to be the consequence of the rotational distortion of the star, which forces the slow precession of a one-armed density wave embedded in the star's equatorial disc (Papaloizou, Savonije, & Henrichs 1992). The mass and approximate density distribution of the disc have been measured from millimeter-wavelength observations out to at least 33 stellar radii (Waters et al. 1991). The disc has been imaged interferometrically in Hα (Mourard, Bosc, & Labayerie 1989; Quirrenbach et al. 1997) and in Hβ (Stee et al. 1998). The latter study gives an orbital obliquity angle of 45° and a disc radius in Hα of $\sim 9R_{\star}$. In order to obtain characteristic velocities of interest, we assumed a $V \sin i = 230$ km s^{-1} (Slettebak 1982), a rotational aspect angle of 45°, and a rotational period of 1.123 days (Smith, Robinson, & Hatzes 1998b, hereafter Paper II). These values lead to an estimated radius of 7.2 $R_{\odot}$ for γ Cas. Next, if we assume a mass of 12 $M_{\odot}$ consistent with its B0.5 spectral type, we may estimate the escape (and infall from infinity) velocity of 800 km s^{-1} at the surface. We measure the terminal wind velocity from the blue edge of the Si IV DAC features as -1800 km s^{-1}.

This series of papers was undertaken with the motivation of understanding the mechanism of X-ray production and its relationship to variability in optical and UV wavelength regions. The primary thrust of our investigation was a simultaneous spaceborne campaign lasting 21 hr on 1996 March 14–15. This campaign was composed of rapid time-series spectra obtained in the region near the Si IV $\lambda\lambda$1394, 1403 doublet with the Goddard High Resolution Spectrograph (GHRS) of the *Hubble Space Telescope* and in the 2–15 keV X-ray region with the *Rossi X-Ray Timing Explorer* (*RXTE*) satellite. Additionally, observations with the *International Ultraviolet Explorer* (*IUE*) were obtained nearly continuously over 33 hr on 1996 January 18–19. In Paper I of this series (Smith, Robinson, & Corbet 1998a), we compared an accurate UV continuum light curve constructed from a relatively "clean" region of the spectrum near the Si IV lines with the *RXTE* X-ray light curve. We found that two minima, having depths of $\sim 1\%$ and separated by 10 hr, which coincide with strong X-ray maxima. Various X-ray characteristics, such as ubiquitous flaring, the short-term nature of color variations, and the coincidence of the extrema in the X-ray and UV light curves, have led to a picture of rotation modulation of the X-ray and UV source regions. By combining the *RXTE* light curve with contemporaneous *ASCA* data (Kubo, Murakami, & Ushida 1999) and *RXTE* data obtained 6 months later, we were able to derive an initial period of 1.125 days for the rotational/activity period. In Paper II (Smith et al. 1998b), we studied the UV continuum (UVC) light curve and compared it to the Si IV line and continuum variations in our January *IUE* data. We found similar dips in the *IUE* data, which enabled us to modify our period estimate to 1.123 days. Several characteristics of these light curves, such as the briefness of the dips and the strong dependence of their amplitudes with wavelength (*IUE* data), together with the absence of predicted spectral signatures of the Si IV lines, have suggested that the UVC dips are caused by at least two optically thin (in the continuum) corotating clouds. Models of the color dependence of the cloud further imply cool temperatures (~ 8000 K). Such temperatures can arise in a plasma cooled by a thermal instability triggered by magnetic heating (see, e.g., Serio et al. 1981). The *IUE* color curves also hinted at the presence of at least one additional cloud present during rotation phases missed in our GHRS observations. This suggests a magnetic topology somewhat more complicated than a simple dipole model.

In this paper we examine the UV spectral variations observed in the GHRS time series. In § 2 we briefly review the observations and reduction procedures. Section 3 then outlines the characteristics of these variations. We leave the analysis of the DACs to a future paper in this series. Herein we concentrate on the study of numerous narrow-bandwidth absorption features, some of which drift in wavelength and others that show a constant wavelength throughout their lifetimes, as well as variations within the cores of the Si IV doublet lines. These observations are interpreted in § 4, where we suggest that they arise from absorbing structures seen in projection against the stellar disc. The drifting features correspond to "cloudlets" tied to the stellar surface by magnetic field lines and forced to corotate with the star. The stationary absorption features appear to arise from blobs that, depending on the sign of their radial velocities, have probably been ejected from regions either near the stellar surface or from the circumstellar disc.

2. OBSERVATIONS

The UV observations were obtained with the Goddard High Resolution Spectrograph aboard the *Hubble Space Telescope* during 13 orbits starting at 21:18 UT on 1996 March 14 and ending at 18:38 UT on March 15. Since we were interested in time variations, the spectra were taken using the RAPID mode of operation, in which short (1 s) exposures were followed by a rapid dump of the data to the tape recorder and the initiation of another exposure. This mode circumvents the full onboard processing that occurs during the more typical ACCUM mode of operation, but it did allow long time sequences of spectra with negligible overhead between exposures. The high declination of the star also allowed us to view it during the satellite's continuous viewing zone. Thus, except for a short sequence of calibrations at the end of each orbit and passages through the South Atlantic Anomaly, our observing timeline was largely continuous. In total, we obtained 1045 minutes of data during the 1280 minute timeline.

The spectra were obtained through the Large Science Aperture (to insure photometric stability) using the medium resolution G160M grating. This setup provided a resolution ($\lambda/\Delta\lambda$) of 10,000 over the wavelength range 1381–1417 Å. This spectral region was selected because it contained the UV Si IV resonance doublet at 1393.80 and 1402.77 Å as well as a region with relatively weak absorption lines, which was used to sample the UV continuum. The Si IV lines were selected for a variety of reasons: (1) they are strong and remain visible over a comparatively wide range of ionization conditions, (2) spectral features seen in one line could be confirmed with the other, thereby reducing the effects of noise, (3) the doublet's wavelength difference provides an essential means for interpreting the radial velocity of plasma having unknown kinematics and ionization states, and (4) the observed ratio of the line strengths provide an indicator of the optical thickness of the line and hence a rough column density of the medium in which it is formed.

Thus, a ratio of 2:1, which is the ratio of oscillator strengths, indicates an optically thin plasma, while a ratio of 1:1 suggests that the plasma is optically thick.

The large UV flux from γ Cas gave a count rate of 8100 counts diode^{-1} s^{-1} in the continuum. The signal-to-noise ratio (S/N) of the observations was therefore limited more by instrumental effects than by counting statistics. The most important of these instrumental effects involved the interaction of the detector's control magnetic fields with the Earth's geomagnetic field. This is often referred to as geomagnetic induced magnetic pertubations (GIMPs) and resulted in shifts of the spectrum both perpendicular and parallel to the detector's diode array, thereby producing changes in observed flux and shifts in wavelength. A complete description of the identification and removal of this and other instrumental effects has been presented in Paper I and particularly in the appendix of Paper II of this series. Briefly, it consists of binning our 1 s exposures to 1 minute averages, identifying groups of pseudocontinuum pixel "windows" in the spectrum outside the Si IV line complex, searching for weak trends in the slope for each spectrum, and dividing the spectra by these trends. This procedure removes most of the spectral dependence of GIMPs. A Fourier filter was passed through the windows along the time axis to remove rapid temporal variations caused by GIMPs.

After removing the instrumental effects, we examined the time sequence for spectral variations having timescales of less than 1 minute. No reliable variations were found over these timescales (see Paper I) so we binned the data into 1 minute averages, both to increase the S/N of the individual spectra and to reduce the number of spectra to a more manageable level. The continuum variations, which were the subject of Paper II, were then removed and a reference spectrum consisting of maximum fluxes for each pixel in the time sequence was subtracted from each spectrum. This reference spectrum was derived from the observations under the explicit assumption that all of the transient spectral variations resulted from spectral absorptions. We note that such a procedure probably underestimates the background stellar flux, since some wavelengths may always suffer some absorption. It is also possible that the presence of variable emission features at some wavelengths would result in spurious absorption components at times when these emission features are absent. Finally, we note that for convenience we have applied a small offset to the GHRS wavelength solution to force the cores of the photospheric Si IV profiles to have a systemic velocity of zero.

3. DATA ANALYSIS

3.1. *Empirical Data Characteristics*

3.1.1. *Initial Data Reconnaissance*

To orient ourselves among the different types of variations in the GHRS data, we refer first to Figure 1*a*. This is a difference image from maximum-flux spectral template such that any variations are by definition in absorption relative to the reference spectrum. The wavelength and time (increasing upward) pixels are in units of 0.07144 Å and 1 minute, respectively. The time series is dominated by strong DAC features, which appear throughout the wavelength region 1386–1400 Å. These are almost exclusively seen in the Si IV resonance lines and have been overexposed in our reproduction of this gray-scale image to bring out the weaker structures both within the photospheric Si IV components and at wavelengths 1399–1417 Å. Except for the DACs, these spectral variations are the subject of the present paper.

From Figure 1*a* it is apparent that nearly all variations (excluding the DACs) can be divided into two basic types. The first remains relative stationary in wavelength, while the second migrates. These basic types can be divided further into four groups. The first group are absorptions present against the cores of the Si IV photospheric lines. These absorptions are strong during the first three spacecraft orbits, then disappear during the middle portion of the observations and reappear during the last few orbits.

A second group are extremely narrow absorptions, which we call "ultrasharp" features (USFs). These are illustrated in Figure 1*b*. The USFs are barely resolved in our 30 km s^{-1} resolution spectra and have lifetimes ranging from 1 to perhaps 10 hr. Most of them appear during the last third of the time series at a wide variety of wavelengths, including within the Si IV profiles, thereby confirming that they are not fixed pattern artifacts. We will further differentiate below between this group and a subgroup of "USF-like" absorptions.

A third group consists of relatively narrow, though still fully resolved, features that drift from blue to red wavelengths at a rate of 95 ± 5 km s^{-1} hr^{-1}. This movement is consistent with the drifts found for migrating subfeatures in optical lines by Yang et al. (1988) and Smith (1995); the latter study determined 92 km s^{-1} hr^{-1}. Therefore, we refer to them as "migrating subfeatures" ("MSFs") in the following discussion. These drifting features are seen in both the 1381–1386 and the 1403–1417 Å regions, that is, at nearly all wavelengths other than those associated with the primary Si IV photospheric and DAC lines. The MSFs maintain their identities from 1 to a few hours. However, for any particular feature the lifetime is difficult to determine because the absorption depths can vary between 0.1% and 0.7%. The MSFs vary through the time series but are visible as a general pattern at all times.

A fourth type of structure appears to show a variable drift, starting as a stationary feature and then rapidly developing a redward drift of approximately the same magnitude as the MSFs. This is a relatively rare type of event and generally lasts 1–2 hr. These features look like curved "ropes" in the gray scale and are brought out in Figure 1*b*. This gray scale depicts two sets of triplet absorptions, spaced 0.55 Å apart, during orbit 9. These patterns are located at wavelengths 1404–1405 and 1410–1411 Å. At present we are unsure of exactly what this phenomenon represents, but we are able to identify the features as arising from S IV and Ni II ions (§ 3.2.1).

3.1.2. *Low-Velocity* Si IV *Absorption Variations within* $\pm V \sin i$

One of the most pronounced spectral features in the time series (aside from the DACs) are the variations against the core of the photospheric Si IV lines. These features remain at roughly constant wavelength but change dramatically in both structure and intensity throughout the time series. This is shown in the mean difference spectra of the 1403 Å line for each of the 13 orbits in Figure 2. In the first two orbits the feature covers a wavelength range of $\sim$1.3 Å and is composed of two or possibly three components. These gradually merge, forming a single structure $\sim$250 minutes into the observation. The feature then fades at 400 minutes

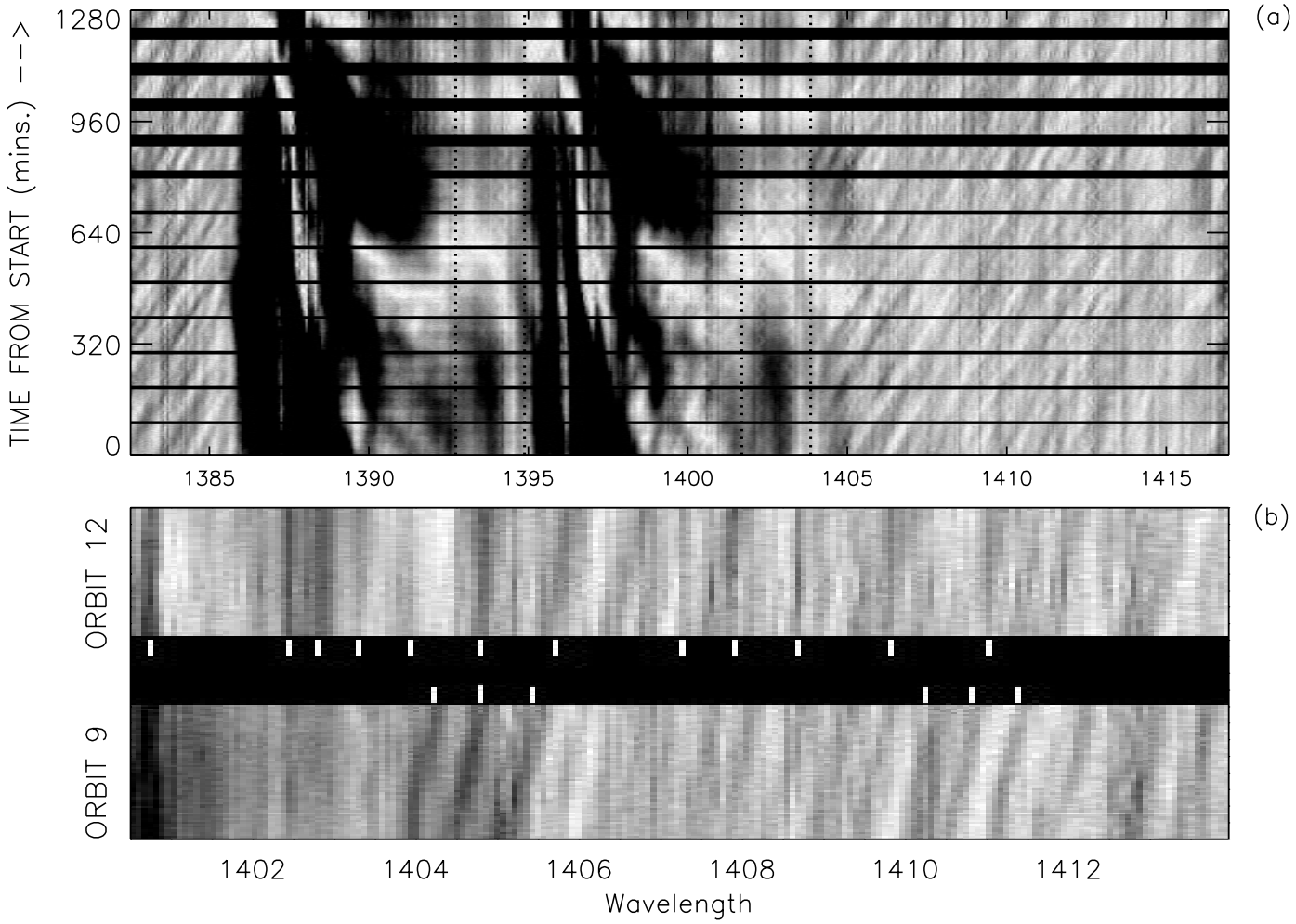

FIG. 1.—(*a*) Gray scale showing the time-series difference spectra of γ Cas taken by the GHRS. Time runs upward and wavelength to the right. Vertical dotted lines show the wavelengths corresponding to the rotational profile limits. The gray scale range was set between −0.03 and 0 of the continuum flux level. The two dark regions in the left-middle portion of the diagram are the Si IV absorption complex from (wind) DAC components. Note the tilted, striated patterns through the extreme blue and red portions of the image; these are the migrating subfeatures. (*b*) Enlarged portions of gray scale for orbits 9 (*lower section*) and 12 in the 1400.5–1414.0 Å region. Several short white lines in the black region show locations of stationary ultrasharp absorption features for orbit 12. Two pairs of white triplet lines denote the presence of two pairs of three "ropes," probably arising from blueshifted S IV 1406 Å and Ni II 1411 Å lines.

and reappears near 900 minutes (orbit 10), again having a multicomponent structure. Note also the prevalence of weak ultrasharp features, which are most prominent late in the observing sequence at -450 km s^{-1} and -75 km s^{-1}. Not surprisingly, the 1394 Å line (not shown) exhibits the same general features. The ratio of flux variations at the same velocities in these two profiles is 1.12 ± 0.03 for the broad core features and 1.05 ± 0.03 within the ultrasharp features. These near-unity ratios imply that the absorbing sources are optically thick.

In Figure 3 we plot the variations in monochromatic flux for points centered on the core of the photospheric Si IV 1403 Å line and at a negative velocity within the profile. We also show the UVC light curve taken from Paper II. The Si IV flux curves show similar shapes and timescales to the continuum curve but appear to lead the latter by about 200 minutes.[3]

[3] We remind the reader that the *IUE* data presented in Paper II shows a probable UVC minimum at a phase coinciding with that of just beyond the end of our GHRS time series.

3.1.3. *The Spectrum of All Variability*

To identify the ions responsible for transient absorption features beyond the limits of the photospheric Si IV profiles, we examined the data using three types of statistical tests. In the first, we determined the total rms scatter within the time sequences obtained from each of 500 separate diodes. We then plotted the value of these rms deviations against the wavelength sampled by that diode. The results are presented in Figure 4 and are similar to the "temporal variance spectrum (TVS)" introduced by Fullerton, Gies, & Bolton (1991) for assessing the significance of spectral variations in time series data. The second type of analysis entails calculating the linear Pearson correlation coefficient for each of the 500 individual time sequences against a reference time sequence obtained near the center of the Si IV 1403 Å spectral line. The larger the correlation coefficient, the more similar are the variations of a given wavelength to variations of the reference wavelength. The third analysis consists of adopting a reference pixel and computing the slope of the linear regression for all pixels in the spectrum. To make this test independent of the second, we chose a refer-

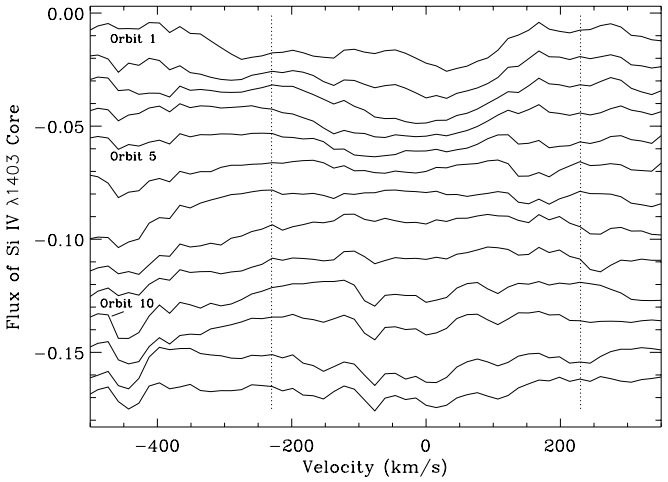

FIG. 2.—Orbit-by-orbit difference spectra for the Si IV 1403 Å line. Individual orbits are displaced by ~1% for clarity. This montage displays the evolution of both a broad, low-velocity core in the range −200 to +100 km s^{-1} and, in late orbits, narrow ultrasharp features over a range of wavelengths, e.g., at −440 km s^{-1} and −80 km s^{-1}. The vertical dotted lines represent the rotational limits of the photospheric line profile.

ence "active" pixel at 1417.0 Å. Flux variations of this wavelength not only showed significant regression slopes with fluxes of wavelengths in the Si IV DACs but also with those wavelengths for which we make line identifications below. Formal significance tests for our regression slope plots show 2 σ significances for slopes greater than $|0.2–0.25|$. A spectrum of regression slopes versus wavelength is presented in the top panel of Figure 5. This plot exhibits broad plateaus at wavelengths corresponding to the Si IV DACs as well as narrow peaks that we will identify with circumstellar plasma lines presently. We also present a plot of the correlation coefficients (test 2) as a function of wavelength in Figure 4. Note the very broad wavelength range of those features near the Si IV line center. These show a correlation coefficient in excess of 0.8 over nearly 1.5 Å and centered at a velocity of about −30 km s^{-1}. This shows that wavelengths throughout the entire line core tend to vary in phase with one another and suggests that the entire Si IV feature originates from low-velocity, ejected circumstellar gas.

Figure 4*b* also shows a variety of narrow correlation peaks that are probably associated with absorption lines other than Si IV. The most pronounced of these features are centered at wavelengths of 1403.8, 1404.5, 1406.1, 1407.6, 1411.7, 1413.0, 1416.8, and 1417.2 Å. In general, these features are in agreement with peaks in the rms spectrum with one exception, a pronounced enhancement in the rms spectrum near 1416 Å, which does not appear in the correlation plot. To examine this feature we generated a second correlation spectrum, in this case using the time variations near 1416 Å as a reference. The results are presented in the upper panel of Figure 5. The peaks in this correlation spectrum are much broader than those in Figure 4, with the most pronounced features occurring in the ranges 1383.0–1383.2, 1403.9–1405.5, and 1415.8–1416.3 Å. As shown in Figure 3, these wavelengths have flux time histories with maximum absorptions at times centered near 200 minutes and 800 minutes, thus showing a morphology similar to the W-shaped form of the moderate velocities along the Si IV profiles.

In § 3.2 we will discuss the identity of the spectral features shown in Figures 4 and 5.

3.1.4. *Spectrum of Variations for Migrating Subfeatures*

As a step toward determining the line identifications and possible systemic velocities of the MSFs, we noted that a typical MSF lasts for approximately 100 minutes at a given wavelength and causes a V-shaped variation in time series of the affected wavelengths. This pattern is quite different from either the W-shaped variations of the Si IV line centers or the slow undulations of the USF features. Accordingly, we wrote a program to compute for each pixel (j) the statistical quantity

$$D_j = \sum_{i=1}^{1000} |f_{j,i} - f_{j,(i+\Delta i)}| \,. \tag{1}$$

Here $f_{j,i}$ is the flux in pixel j at time i and Δi is a time difference roughly equal to one-half the lifetime of the variation, i.e., about 50 minutes. Since the absolute values in this accumulation process are positive, the final sums are a

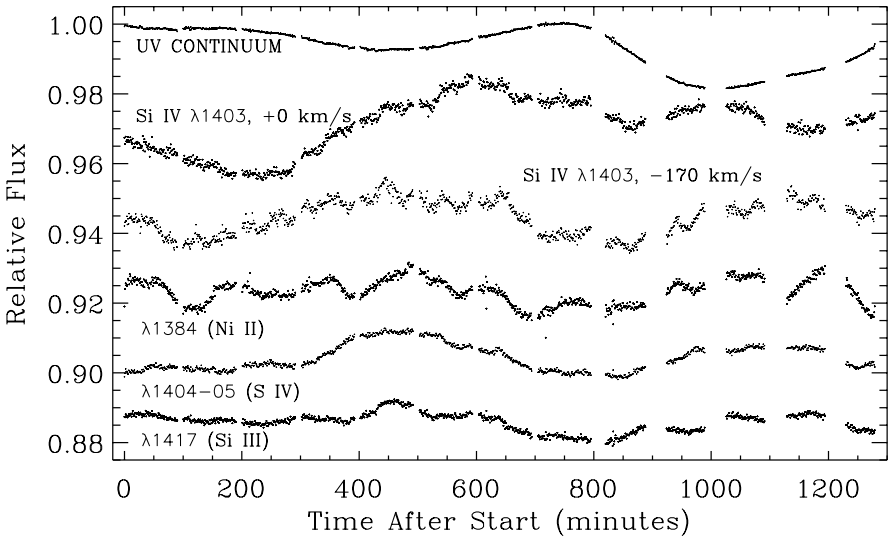

FIG. 3.—Time series of fluxes for the UVC, the Si IV 1403 Å line at 0 and −170 km s^{-1}, and at −170 km s^{-1} for the nearby Ni II, S IV, and Si III lines. The V-shaped features in the fluxes of the Ni II line are caused by migrating subfeatures.

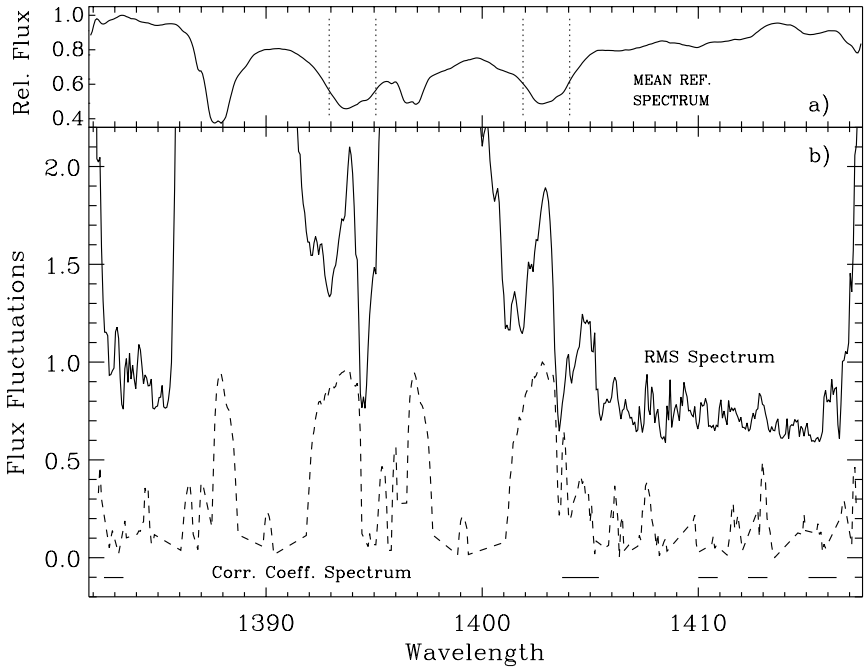

FIG. 4.—(*a*) Mean spectrum from the GHRS data. Dotted vertical lines represent rotational limits on the photospheric Si IV lines. (*b*) Comparison of spectra computed from the average rms flux fluctuations of wavelengths along the spectrum (*solid line*) and from the cross-correlation of the fluxes with respect to the center of the Si IV 1403 Å line (*dashed line*), except that negative cross-correlations have been deleted in the interest of clarity (see Fig. 5). The rms spectrum has been multiplied by 200 and offset by +0.2 units. Horizontal lines indicate wavelengths of activity in the rms spectrum attributable to Ni II, S IV, and S III.

measure of variability tuned to the characteristic time of the MSF's V-variation. When repeated for all 500 pixels along the spectrum, this procedure produces an activity spectrum that is sensitive to the presence of MSFs and other possible short-lived transients. Figure 6*b* exhibits a series of spectra computed for time shifts of 40, 50, and 60 minutes; the mean spectrum is shown for reference in the upper panel. The similarity of these three spectra shows that their details are generally insensitive to the precise time lag adopted within this range. However, the clear features in these spectra disappear for time shifts significantly outside this range, imply-

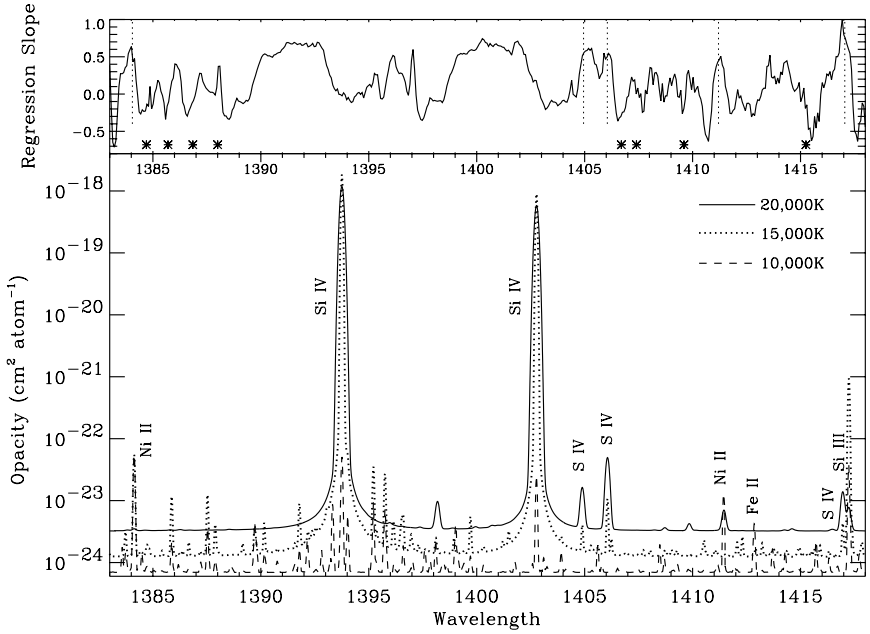

FIG. 5.—*Upper panel*: Regression slopes of fluxes along the spectrum with respect to the flux in the Si III 1417 Å line (*rightmost dashed line*), shifted by +0.8 Å to bring it into the rest frame of the panel below. Dotted lines show the coincidence in wavelength of these cool-gas lines with features for which fluxes correlate positively with those of Si III λ1417. Starred symbols denote the positions of the Fe V lines identified in hot-plasma features (cf. Fig. 7). Their coincidences with negative correlations are evident. The regression slope measure of pixel-to-pixel correlations agrees very well with the correlation coefficients shown in Fig. 4. *Lower panel*: Opacity spectra calculated for temperatures 10,000 K, 15,000 K, and 20,000 K and $N_H = 10^{11}$ cm^{-3} in the wavelength region of the GHRS spectra; the latter two are offset for clarity. Identified lines in this spectrum are those found to exceed the empirical detection limit of 1×10^{-23} cm^2 atom^{-1}.

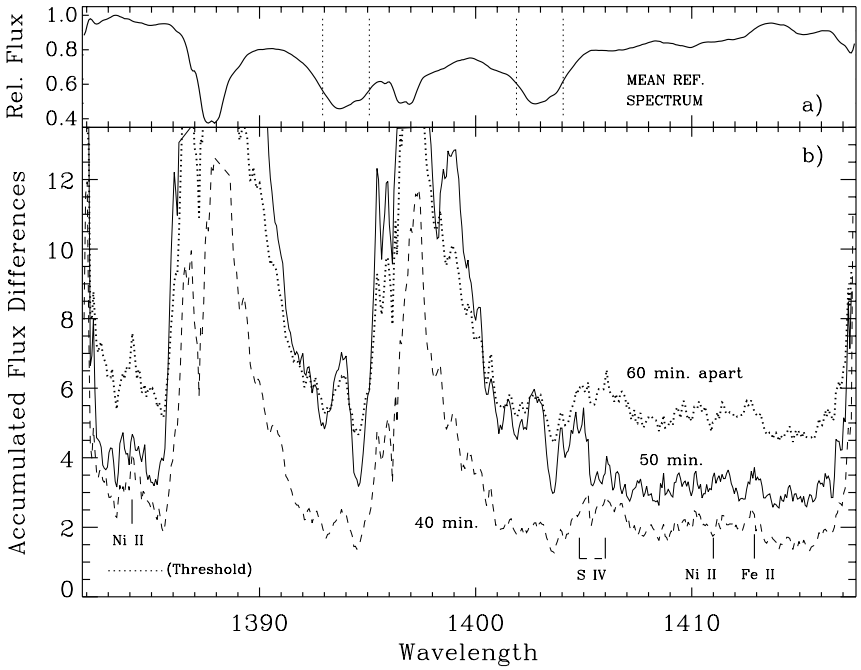

FIG. 6.—(*a*) Mean spectrum once again. Dotted vertical lines represent rotational limits on the photospheric Si IV lines. (*b*) Spectrum of the average accumulation of absolute values of flux differences for pixels separated by 40, 50, and 60 minutes. Ordinate values are accumulated flux differences over 1045 spectra in normalized continuum units. The latter two spectra are shifted upward by 1 and 3 units. This V-signal is sensitive to migrating subfeature (MSF) absorptions in the flux time series. Peaks are due to MSF absorptions from lines of Ni II, Si III, and S IV. The estimated level of variability by sources other than MSFs is indicated as "threshold." The fact that the observed fluctuations are well above this floor indicates that virtually all wavelengths outside the Si IV complex are affected by MSFs.

ing a characteristic variation over ~100 minutes for most wavelengths outside the Si IV lines. We add the caveat here that additional inspections of time series at many wavelengths revealed that for wavelengths near 1415 Å the accumulation sums were dominated by a rapid-jitter signal rather than by the MSFs. We return to this point in § 3.4.3.

3.2. *Line Identification of the Features*

3.2.1. *Identification of Lines from Warm Circumstellar Plasma*

To identify lines from the variability spectra determined from the rms's, cross-correlations, and MSF sums, we used the SYNSPEC radiative transfer program (Hubeny, Lanz, & Jeffery 1994; I. Hubeny 1996, private communication) to generate opacity distributions as a function of wavelength for a fine grid of isothermal absorbing slabs with temperatures ranging from 6,000 to 100,000 K. Hubeny, Heap, & Lanz (1997) have used these codes and line list to synthesize the 1460–1500 Å spectrum of 10 Lac (O9 V). They find a very high success rate (~97%) in predicting the appearance of spectral lines. In most cases these opacities were insensitive to the other primary inputs of slab density (set to 10^{11} cm^{-3}) and microturbulence (25 km s^{-1}). We then compared these opacities with the enhancements of the various statistical quantities presented in Figures 4, 5, and 6. An example of this comparison is shown in the upper panel of Figure 5. This plot shows that the identified cross-correlation enhancements identified from the 1416.0 Å reference sequence correspond to lines of Ni II λ1384.1, S IV λ1404.7 and λ1406.1, and Si III λ1417.2 (blended by S IV λ1416.9). In each case these features are all shifted by −170 km s^{-1} relative to the zero velocity determined from the positions of the Si IV line cores. All of these lines are formed over the temperature range from 10,000 K to 18,000 K and will henceforth be referred to as "warm plasma" lines.

A similar comparison to the correlation spectrum shown in Figure 4, which used the low-velocity Si IV time series as a reference, also identifies the S IV 1404.7 Å and 1406.1 Å, S IV 1416.9 Å, and Si III 1417.2 Å lines, except that here they are blueshifted by only 20 ± 10 km s^{-1}. Thus, we have evidence for at least two separate structures. The first is associated with an outflows with a range of at least 100 km s^{-1} around a mean of −170 km s^{-1}. The second structure produces the low-velocity Si IV variations and has outflow velocities over a small range centered at −30 km s^{-1}.

In Figures 4 and 6 we were also able to identify the presence of the Fe II 1412.9 Å line, which was is not visible in the blueshift-sensitive spectrum of the upper panel of Figure 5. According to our opacity distributions, this line is visible for only the narrow range of plasma temperatures 8300 ± 700 K. The behavior of this line is similar to the warm plasma lines in that it always lies within $\pm V \sin i$ of its mean velocity, but unlike the warm group its velocity is near zero. As we will show in (§ 3.4.3), it also shows a different variation with time from the warm-plasma lines.

3.2.2. *Identification of Lines from Hot Circumstellar Plasma*

Our next step in line identification was to examine the many USF features. Because of their stationary positions there was little ambiguity in their observed wavelengths. We again used our temperature grid of opacity distribution functions to search for features with the same spacings as those in our difference spectra. We began with the warm-plasma ions mentioned above but had little success in matching observed features except for Si IV itself. However, examining higher temperature slabs led to a set of mainly

Fe v lines at 1402.3, 1406.7, 1409.4, 1415.1, and 1418.1 Å (if blueshifted, the 1418 Å line is visible at the red edge of our spectra), which provided acceptable matches to the observations. These lines peak at $T \sim 45{,}000$ K but are visible for plasma temperatures of 32,000–50,000 K and attain the same strength as the Si IV doublet at $T = 34{,}000$ K. We note that these wavelengths are those for which negative cross-correlations were found in the upper panel of Figure 5. This fact suggests that the hot- and warm-plasma regions in which the lines are formed are not cospatial. By adopting the Si IV and Fe V wavelengths and Doppler shifting them by various discrete velocities, we were immediately able to match positions and relative strengths of features in various spectra in our time series with confidence. Figure 7, the average spectrum of orbit 13, shows one of several possible examples. The features shown at these times are also apparent in spectra of different subsections of orbit 13 as well as over the last few orbits. We were able to match virtually all the observed features with 14 self-consistent velocity systems. In this plot the arrows represent the position of an Si IV 1403 Å feature that coincides in position and strength with an Si IV 1394 Å feature shifted by +9.0 Å. These particular systems do not show traces of Fe V absorptions, so we attribute them to warm circumstellar structures. The combs in Figure 7 designate the positions of Si IV and nearby Fe V lines at the same velocity. These arise from hot structures ($T > T_{\rm eff}$). The presence of the DAC features below 1400 Å interferes with the identification of systems with velocity more negative than −430 km s^{-1}. In all, the velocity systems identified extend to at least $\sim +1500$ km s^{-1}. Corroborating evidence for the large number of velocities needed for these identifications is given in the following section.

3.2.3. *Further Support for the Warm- and Hot-Plasma Line Identifications*

To check further on the line identifications and velocities we determined for the transient spectral features, we developed a statistical algorithm that searches through the time series for absorption features that are separated by a predetermined wavelength separations corresponding to the difference between two related spectral lines. Thus, for example, we computed the cross-correlation coefficient between the fluxes from 9 pixels centered at various positions in a spectrum with a similar group located 9.0 Å (126 pixels) to the red in order to search for structures caused by the Si IV doublet. This procedure was repeated for all spectra in the series. By plotting the value of the correlation coefficient versus the wavelength and time of the reference pixel, we produced a velocity versus time map in which high correlations could be flagged.

As might be expected, the map tuned to the Si IV line separation reproduced the blueshifted DAC features extremely well, as well as an abundance of fine structure at redshifted wavelengths. Unfortunately, repetition of this procedure with random wavelength spacings also produced maps containing isolated occurrences of spurious high correlations that arose from chance coincidences of subfeatures with variations of the 1403 Å DAC and with unrelated features (noise or otherwise) longward of 1403 Å. This fact meant we had to rely upon a more indirect approach to demonstrate that these maps contained relevant information on the subfeatures.

Our procedure was to compute histograms of the incidence of correlation coefficients for all observed times for over 20 trial wavelength separations. We found that these histograms could be segregated into two groups, with the first showing an excess of incidences of high correlations relative to the second group. We found that members the high-correlation group coincided with one or the other of the wavelength separations listed in Table 1 to an accuracy of ±0.1–0.2 Å. Similarly, the histograms with smaller incidences of high correlations all had separations different from Table 1 values. As examples, we exhibit in Figure 8 four histograms, each within a velocity range specified, of correlation coefficients computed from a discrete wave-

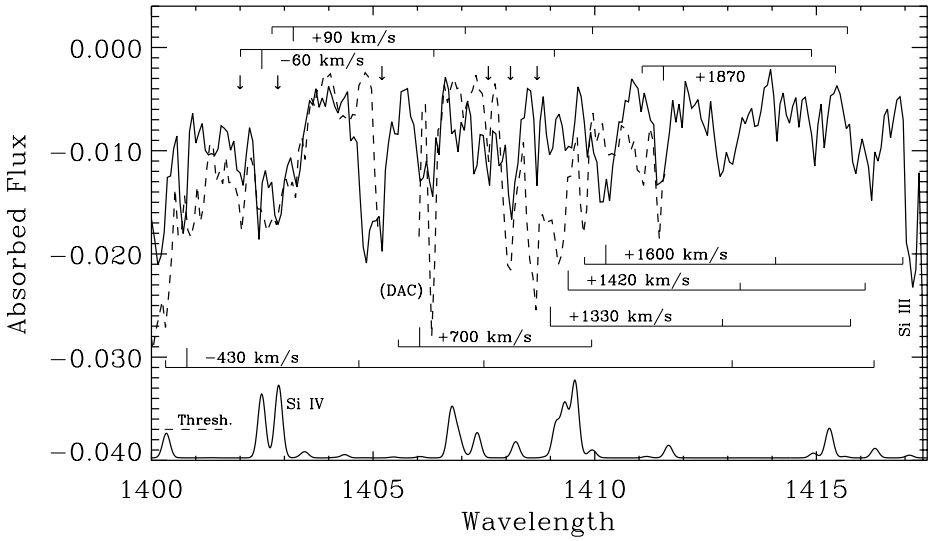

FIG. 7.—Identification of sharp, stationary features in the red portion of our GHRS difference spectrum for orbit 13 (*solid line*). The dashed line is the same spectrum near Si IV 1394 Å shifted by +9.0 Å. This line can be compared with the solid line to search for matches of Si IV features over a range of moderate velocities. Arrows denote matches only for Si IV and mark the effective Doppler shifts relative to the rest frame at 1402.8 Å. The combs represent blue- and redshifted systems at the indicated velocities. In these cases matches can be found for the Si IV doublet lines (*long vertical tics*) and the Fe V lines at 1402.3, 1406.7, 1409.4, and 1415.1 Å (*short tics*), i.e., warmer material. The emission lines at the bottom are the calculated opacity spectrum for 34,000 K. This spectrum is shifted by +0.1 Å to match features in the upper panel. With one exception (the line attributed to Si III), all identified features are due to Si IV or Fe V lines.

TABLE 1

SEPARATION OF CANDIDATE LINE PAIRS ABSORBED IN CIRCUMSTELLAR BLOBS

Blue Line in Pair	Red Line in Pair	$\Delta\lambda$ (Å)	ΔPixels
Si IV λ1394.8	Si IV λ1402.8	9.0	126
Fe V λ1402.3	Fe V λ1406.7	5.0	61
Fe V λ1402.3	Fe V λ1409.4	7.1	98
Si IV λ1402.8	Fe V λ1406.7	3.9	55
Si IV λ1402.8	S IV λ1406.0	3.2	45
Si IV λ1402.8	Ni II λ1411.0	8.2	115
S IV λ1406.0	Ni II λ1411.0	5.0	70
Ni II λ1411.0	Si III λ1417.2	6.2	84
Fe V λ1415.1	Fe V λ1418.1	3.2	45

length shift listed in Table 1. In each panel the shaded area bounded by upper and lower dashed lines represents the range of correlation coefficients for a set of 10 random shifts, that is, shifts falling in between those listed in Table 1. The dashed lines may be thought of roughly as confidence belts of $\pm 1.7\ \sigma$ significance for these random-separation trials. These histograms demonstrate that the solid lines uniformly fall above these belts for correlation values above ~ 0.85. This indicates a real detection of the specified line pair within the velocity range sampled by the histogram. Note especially that the degree of Si IV line successes (*thick solid line*) falls off quickly with velocities above $+600$ km s^{-1} but has a small persistent excess for velocities even above $+2000$ km s^{-1}. This is in agreement with the identification of velocities at $\sim +1500$ km s^{-1} in Figure 7. Although the test does not differentiate between the types of features (USF vs. MSF) responsible for the excess high cross-correlation coefficients, our inspection and matchings of individual features in the spectral series suggests that the USFs are responsible for features with velocities >300 km s^{-1}.

3.2.4. *Additional Cool-Plasma Lines Identified*

As a postlude to the identifications of lines in our own data, we were able to make use of archival high-quality GHRS echelle data at a nearby wavelength region obtained

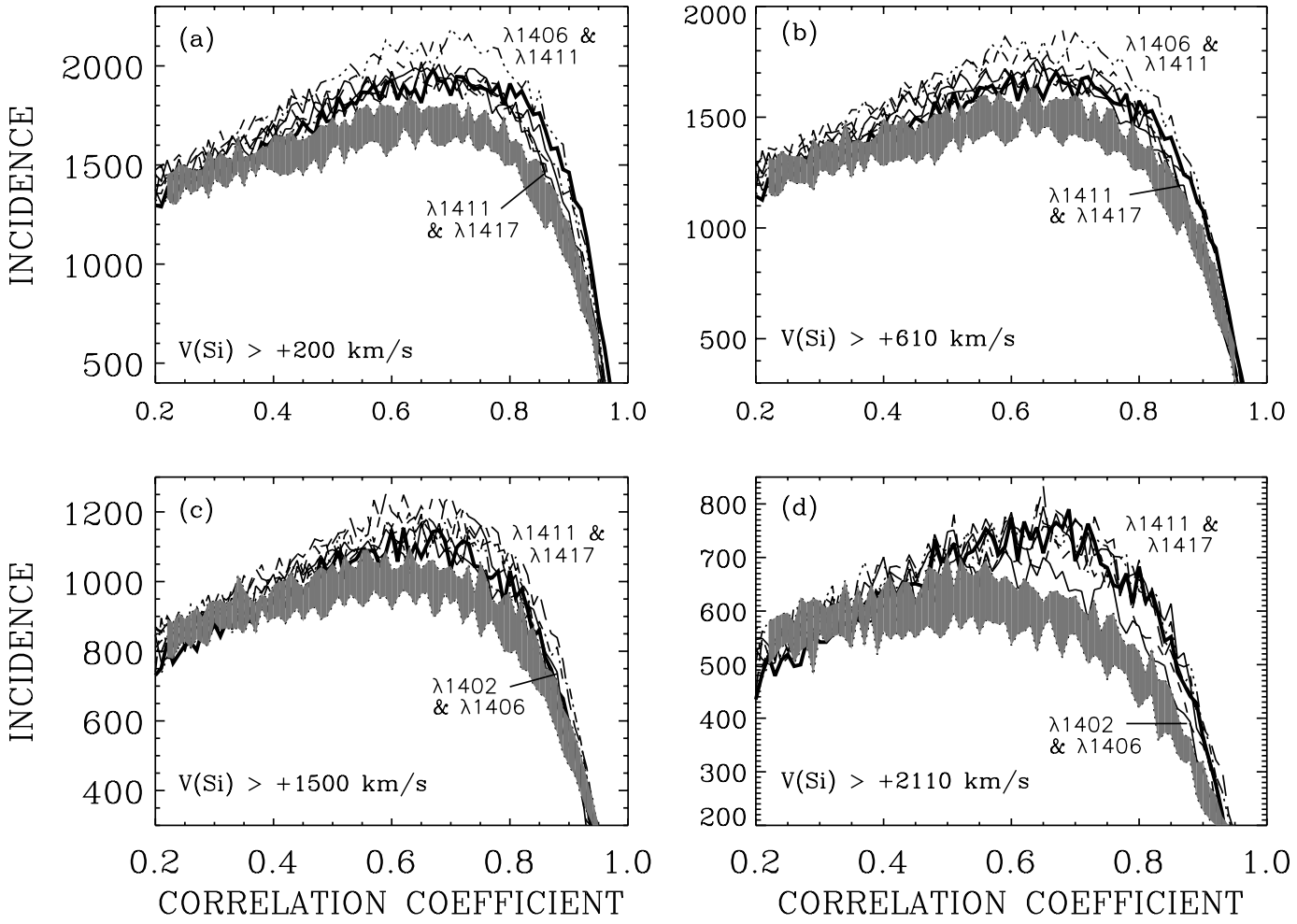

FIG. 8.—Histograms of cross-correlations for pixels in the difference spectra with respect to a pixel n Å to the red of that pixel, where n is the wavelength spacing of candidate line pairs (Table 1). Correlations of pixels corresponding to the spacing of the Si IV doublet are shown as a bold line. The thatched area corresponds to the total range ($\pm 1.7\ \sigma$) of cross-correlations for random spacings of pixel pairs, i.e., the distributions of cross-correlations expected by chance. The lower velocity limit given refers to the Si IV 1394 Å line with respect to its companion line at 1403 Å. This velocity limit will differ for each line pair according to the first member's wavelength. The four panels refer to different wavelength regions in the spectra starting at $+0.9$ Å, $+2.9$ Å, $+7.0$ Å, and $+9.9$ Å and end at $+26.3$ Å, $+28.3$ Å, $+17.7$ Å, and $+17.7$ Å, relative to the systemic-frame core of the Si IV 1394 Å line. Line pairs showing the highest and lowest cross-correlations are identified. Note that the highest correlations correspond to the higher wavelength line pairs as one searches redder wavelengths regions in each successive panel. The Si IV doublet continues to show high correlations for velocities >2000 km s^{-1}, indicating circumstellar matter at high infall velocities.

by Meyer, Jura, & Cardelli (1998) for a program designed to measure the strength of the interstellar O I 1356 Å line. These authors were kind enough to provide us with the nearly 7 Å of their original "snapshot" spectrum of γ Cas.[4] This is presented in Figure 9. The spectrum shows a series of 0.3–0.4 Å wide, faint absorption features at several wavelengths. These features have the same characteristic widths and depths as migrating subfeatures observed in the optical and in our own GHRS spectra. We therefore proceeded to identify them with opacity distributions computed with the SYNSPEC program. The simulations for this wavelength range had temperatures of 7000–20,000 K and a density of 10^{11} cm^{-3}. We were able to identify most of these features with four lines due to Si II λ1352.6, Ni II λ1353.8, O I λ1355.9, and Fe II λ1359.0, all redshifted by $\sim +160$ km s^{-1}. Using the period of 1.123 days from Paper II, we find that the Meyer et al. observations were taken at the phase corresponding to orbit 11, which occurred just before the UVC curves decreased to their minima fluxes. The appearance of cool-plasma features from Fe II, Si II, and C I at the time of the passage of a cool cloud adds credence to our line identifications. It demonstrates by arguments independent of those used in Paper II that the corotating clouds producing the minima in the UVC light curve have temperatures less than 10,000 K.

3.3. *The Possibility of Emission Features*

In the previous analysis we have referenced the data to a spectrum in which the flux at each wavelength corresponds to the maximum flux observed at that wavelength during our observations (see § 2). This forces all transient features in the residual time series to appear as absorption features. To investigate the possibility that some features are in emission, we generated a second time series in which the reference spectrum contained the minimum observed flux. The corresponding gray scale (not shown) shows weak emissions (e.g., during orbit 13) at the rest frame locations of Si IV, the major Fe V lines identified in Figure 7, and at the locations of the warm-plasma lines of Ni II, S IV, and Si III. These results are consistent with the conclusions that both groups of lines are optically thick. It also hints that the structures forming these features are nonuniformly distributed in rotation phase. However, we are aware that interpreting difference spectra from a minimum spectrum template can be risky if there is no independent evidence for emission. For example, emission features can arise as artifacts of the absence of absorption at other times. For the present we conclude that these findings are consistent with the expected presence of emission from optically thick clouds, but we are reluctant to cite this as independent evidence.

3.4. *Characteristics of Lines Formed at Different Temperatures*

3.4.1. *Phasing between the UVC Light Curve and Warm-Plasma Absorptions*

A general property of the warm plasma features including those within the photospheric Si IV lines is that although they are well correlated with each other, they "lead" the UVC light curve by about 200 minutes. This behavior is depicted in Figure 3. Moreover, the variations of the S IV wavelengths are actually anticorrelated with the UVC light curve. This is shown in Figure 10, which exhibits the run of absorptions of λλ1404.8–1405.5 against the decreases in the UVC curve. This plot shows two discrete "branches," which correspond to the passages of the first and second continuum flux minimum in orbits 1–8 and 9–10, respectively. In Paper II we demonstrated that these minima are probably produced by clouds forced into corotation above

[4] These observations were a series of three ACCUM observations made on 1995 October 31 at 16:15–16:37 UT. During this time any MSFs would be expected to drift by only 32 km s^{-1}. As this is still less than their intrinsic width, coaddition of these spectra produces at most only a small smearing of their profiles.

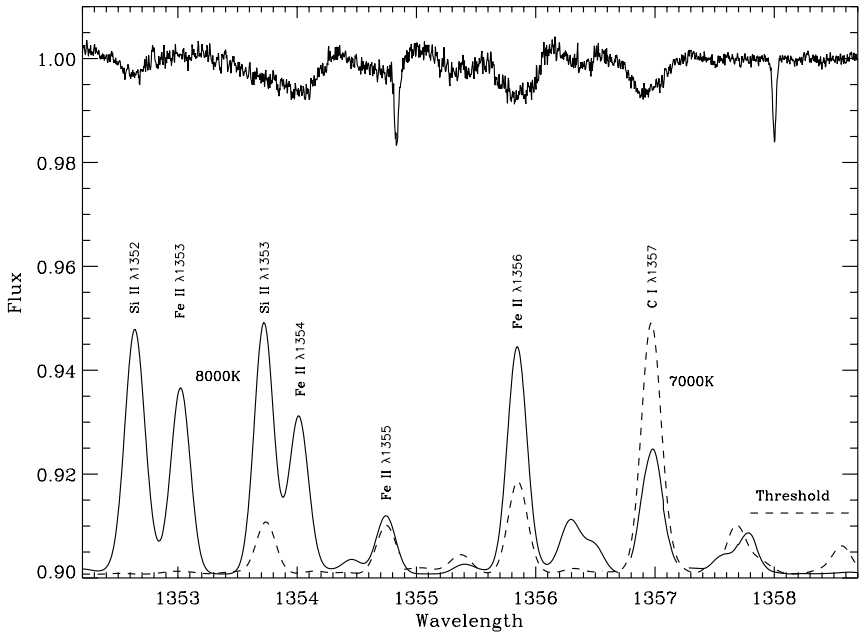

FIG. 9.—Reproduction of the snapshot spectrum of the region surrounding the interstellar O I 1355.8 Å line obtained by Meyer et al. (1998). Note the faint absorption dips with widths of 0.3–0.4 Å, which are probably migrating subfeatures. The spectrum has been shifted by −0.75 Å to match the laboratory frame of the opacity spectra (*bottom spectrum*) for 7000 K and 8000 K. The dashed line in the lower left is the opacity detection limit of 10^{-23} cm^2 atom^{-1} taken from Figs. 4 and 5*a*.

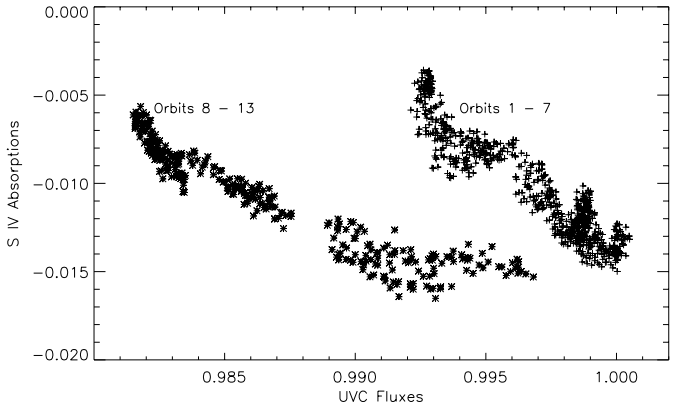

FIG. 10.—Absorptions of the S IV line absorptions at 1404.8–1405.5 Å vs. UV continuum fluxes determined in Smith et al. (1998b). The two fluxes are anticorrelated and follow distinct branches for the early and late *Hubble Space Telescope* orbits, corresponding to observation start through 795 minutes and 820 minutes to the end.

the star. The two different trajectories followed by these fluxes can be most easily interpreted as two separate phase lags between two clouds absorbing UVC flux and different circumstellar structures that absorb radiation in the warm-plasma lines.

3.4.2. *Comparison of Migrating and Ultrasharp Subfeatures*

With some sense finally made of the complex identifications from warm- and hot-plasma lines, we can discuss the short-term character of MSF features. Figure 11 shows a typical example of a MSF seen redward of the Si IV lines during orbit 3. One sees that what appears to be a single MSF feature in the gray scale is actually a cluster of individual narrow components. The ensemble of cool-plasma components indeed moves at the rate determined from the analysis of MSFs in the Figure 1 gray scale. However, the individual subfeatures have much shorter lifetimes than inspection of the gray scale could suggest. Typically, a new component forms to the blue or red of an old one. The new feature then broadens and decays, typically in much less than 100 minutes. These characteristics are especially pronounced in observations taken during the first few orbits.

The identifications in Figure 11 show that variable absorption features seen early in our observations may arise from either warm- or hot-plasma lines. However, there is a key difference between these two groups: features originating from warm-plasma lines, aside from the Si IV doublet, clearly migrate redward, whereas features arising from hot-plasma lines do not. In a detailed inspection of Figure 11, we were not able to find a single clear case for which the S IV, Ni, II, or Si III lines migrate from their mean velocity by more than $\pm V \sin i$. In contrast, the Si IV features appear at high Doppler shifts and, along with the Fe V lines, comprise the stationary USF patterns, which may extend over a moderate range of Doppler shifts. In addition, transient clusters of low-velocity features due to both Si IV and Fe V are visible early in the observations. These latter features resemble the USFs in some respects, so we will designate them "USF-like." However, there are two distinctions between USF-like and USF absorptions. First, the USF-like absorptions appear in closely spaced aggregates of components and do not show ready evidence of appearing over a wide velocity range ($\geq$1000 km s^{-1}). Second, they are the most dynamic group of features of all, even more so than the

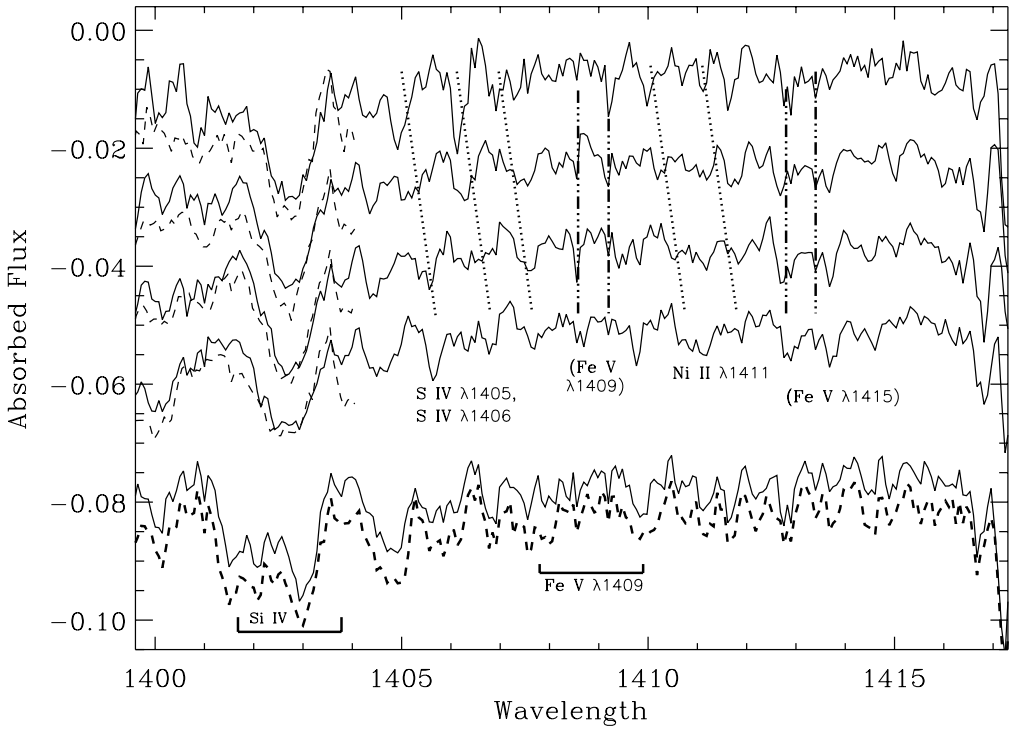

FIG. 11.—Depiction of the rapid evolution of individual MSF features in orbit 3. First four spectra are 3 minute averages on March 14 at 00:49, 01:21, 01:53, and 03:25 UT. Diagonal dotted lines show the redward migrating subfeatures from warm-plasma lines of S IV (two) and Ni II (one). Vertical dot-dashed lines are stationary features arising from Fe V lines identified in parentheses. These dots follow two different velocity systems except that two of the four components of the two S IV lines overlap. The lower pair of spectra were taken on March 14 at 21:40 and 21:45 UT. The combs under them show a pair of features that broaden perceptibly in this five minute interval. The Si IV 1394 Å line (not shown) exhibits features with the same rapid broadening.

MSFs. As one example, the lower pair of spectra in Figure 11 shows the evolution of two pairs of features, due to both Si IV lines and Fe V λ1409. These appear at velocities ∼450 km s^{-1} apart. Remarkably, these features broaden perceptibly *in 5 minutes* in the lower spectrum. Adjacent spectra in time to those shown exhibit this same ultrarapid broadening.

In Table 2 we summarize the defining characteristics of the MSF, USF, and USF-like absorption components.

3.4.3. *Time History of Features at* 1413–1415

The dynamic quality of the USF-like features (§ 3.4.2) led to the discovery that these features can occasionally influence the statistics of the time-paired flux variations that we had initially attributed to the MSFs (Fig. 6). Additional analysis disclosed that in most wavelengths the MSFs dominate the ephemeral changes of the USF-like absorptions, but that the USF-like activity can be dominant in the narrow region of 1414–1415 Å. To examine whether these features could be related to the MSFs, and therefore whether the USF and MSFs are formed in similar regions, we decided to determine this time for specific wavelength bins the sums calculated in equation (1) over $\Delta i = 40$, 50, and 60 minutes. We found that, whereas the MSFs dominate the sums in the wavelength range 1413–1414 Å, short-term fluctuations dominate the sums for 1414–1415 Å.[5] As in the construction of Figure 6, we accumulated the flux differences. However, this time we tabulated the mean accumulations per minute within each orbit and binned the results over these two wavelength ranges. The sets of time histories for the two wavelength bins looked very similar compared to the orbit-to-orbit fluctuations with each, so we took their averages. The resulting time histories of fluctuations are displayed in Figure 12, again for values $\Delta i = 40$, 50, and 60 minutes. The plot shows weak peaks at 0 and 1000 minutes in each of the three trials and a stronger 400 minute peak. We found it difficult to formulate a formal test of significance for two reasons. First, nonrandom variations are present in our data, particularly at short timescales. Second, smaller circumstellar clouds may also exist at various positions over γ Cas. Although we cannot estimate a significance level accurately, we can point out that each of the three peaks coincides with the times of the passages of cool clouds in front of the star according to the UVC light curves (including the *IUE* data). Moreover, a visual inspection of Figure 1*a* shows the 400 minute peak and a dearth of MSFs near 300 and 500–600 minutes. The likely identifications for the absorptions near 1413 and 1415 Å are the Fe II 1412.9 Å (identified already from Fig. 6) and Fe V 1415.1 Å lines. Thus, the peaks in Figure 12 imply that both cool and hot plasma absorptions correlate with the occurrences of the dips in the UVC curve. We have verified this result by comparing the time series at 1415 Å with the UVC light curve and finding that the two curves are well correlated. From these results we conclude that it is likely that the cool and hot plasma regions are somehow associated with one another, but they are probably not cospatial.

[5] We also remind the reader that the second wavelength range also shows negative cross correlations in the upper panel of Figure 5.

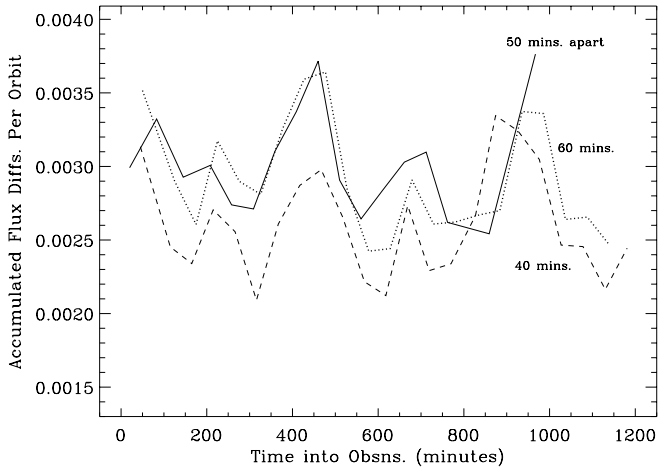

FIG. 12.—Orbit-by-orbit time history of accumulation of V-signature from times 40, 50, and 60 minutes apart in the wavelength range 1413.0–1415.5 Å (Fig. 6). These accumulations are sensitive to ephemeral variations from the USF-like features. The 50 minute curve does not continue to late times because of chance interorbit gaps in the data train, which preclude continued 50 minute sampling. Peaks occur for each of the trial curves at ∼500 and ∼1000 minutes, corresponding to the passages of the cool clouds.

4. INTERPRETATION

4.1. *The Migrating Subfeatures*

The MSFs in the UV lines of γ Cas have characteristics similar to the blue-to-red patterns observed in the Hα line on the active K0 V star AB Dor (Cameron-Collier & Robinson 1989). The most likely explanation is that these features arise from dense clouds of plasma trapped in magnetic loops above the star's surface and are forced to corotate with the star. This plasma appears to be at a temperature consistent the radiative temperature with matter at the top of the atmosphere in γ Cas. It is also much more dynamic than in AB Dor, since the individual drifting bands are broken up by highly variable fine structure.

As discussed in Cameron-Collier & Robinson (1989), the average height of the cloud ($R_{\rm cloud}$) can be determined from

TABLE 2

CHARACTERISTICS OF ABSORPTION FEATURES

Feature Type	Temperature [Ion] (kK)	Velocity Range (km s^{-1})	Acceleration?	Lifetime (minutes)
MSF	COOL (≤10) [O I, Si II, Fe II, Ni II]	$\pm V \sin i$	Yes	Subcomps: several Clump: 60–180?
	WARM (10–18) [Ni II, Si III, S IV]	(same)	(same)	(same)
USF	WARM (10–18) [S IV, Si III, Si IV, Fe V, Ni II]	$\pm 1500^{+}$	No	60–600
	HOT (30–40) [Si IV, Fe V]			
USF-like.....	HOT (30–40) [Si IV, Fe V]	$\pm 300^{+}$	No	5–30

the drift rate ($d\lambda/dt$) of the migrating feature through the relation

$$\frac{R_{\rm cloud}}{R_\star} = \frac{c}{\omega\lambda V \sin i \cos\theta}\frac{d\lambda}{dt}, \quad (2)$$

where ω is the star's angular velocity, $V \sin i$ is the projected equatorial rotation velocity, θ is the cloud's latitude, and λ_0 is the rest wavelength of the spectral line. In the case of γ Cas the drift rate is on the order of 0.44 Å hr^{-1} (95 km s^{-1} hr^{-1}). Using this with the parameters $V \sin i = 230$ km s^{-1}, $\theta = 45°$, $\lambda_0 = 1403$, and $\omega = 0.23$ rad hr^{-1}, one can determine a height $R_{\rm cloud} = 2.5R_\star$ (relative to the star's center).

To better understand the physical properties of the cloudlets over γ Cas, we have modeled them with the CIRCUS computer code described by I. Hubeny (1996, private communication) and Hubeny & Heap (1996). This program allows the user to simulate the effects of a homogeneous, isothermal cloud of specified size, temperature, density, turbulence, and column mass when seen against a stellar background. In this program the surface of the star is divided into a grid and the spectrum from each point on that grid is calculated in LTE using a standard Kurucz atmosphere (Kurucz 1993) appropriate to the effective temperature and gravity of that star (for γ Cas we assume $T_{\rm eff} = 28{,}000$ K and $\log g = 4.0$). This process automatically accounts for limb darkening effects. A cloud is then specified at a given position with respect to the center of the star and an integrated, rotationally broadened spectrum is calculated. By comparing this spectrum with one calculated without a cloud, the residual effect of the cloud can be determined.

To start the calculations, we assumed that the cloudlets responsible for the MSFs are smaller than the star and have temperatures of $\sim$18,000 K (see § 3.2.1). Since the MSFs appear in the S IV (1404.7 and 1406.1 Å) lines, one expects that the optical depth in these lines should be near 1. Then from the line opacity tables this condition implies that the maximum optical depth for S IV λ1404.7, the weaker of the two S IV lines, is $\tau_{1404} \approx 2 \times 10^{-23} N_{\rm H}$, where $N_{\rm H}$ is the column density of hydrogen atoms. Thus, the likely $N_{\rm H}$ for the cloudlets is $\sim 5 \times 10^{22}$ cm^{-2}. Next, in order to produce the observed 2% absorption feature, the CIRCUS simulations predicted that a marginally optically thick cloudlet located above the center of the star should require an area of $\sim$5% of the projected stellar area ($A_\star$) to produce the observed 2% absorption feature. This implies that the cloudlet has a radius of $\sim 0.2R_\star$. Assuming that the cloudlet is symmetrical and taking $R_\star = 7.2\,R_\odot$ then implies that the cloudlet density should be on the order of 2×10^{11} cm^{-3} and that the total mass of the cloud is $\sim 2 \times 10^{21}$ g (or $10^{-12}\,M_\odot$). These parameters are similar to the values found for the cool clouds studied in Paper II and which we concluded in § 3.4.1 are spatially distinct from the warm cloudlets.

The strongest spectral features within our wavelength region are the Si IV resonance lines. For the temperature of 18,000 K considered above, the optical depth of these lines is given approximately by $\tau_{\rm Si\,IV} \sim 2 \times 10^{-18} N_{\rm H}$. Thus, with the column density of 5×10^{22} cm^{-2} deduced from the S IV absorption, we estimate that the clouds would have an optical depth at line center of 10^5. At these high opacities the pressure broadening induced by the relatively high cloud density ($\sim 2 \times 10^{11}$ cm^{-3}) becomes important, and the features are expected to absorb over a wide range of wavelengths in their wings. To investigate the expected behavior of the Si IV absorptions features, we used the CIRCUS program to simulate the passage of a corotating cloud across the surface of the star. In this simulation we assumed for convenience that the rotation axis was perpendicular to the line of sight and that the cloud was located over the stellar equator. We then calculated a series of spectra in which the cloud was offset from the star center by distances ranging from $-1.0R_\star$ to $+1.0R_\star$. The radial velocity of the cloud was determined from the well known fact that the line-of-sight velocity for any point on a solidly rotating sphere is dependent only on the x-displacement from the rotation axis. Thus, a corotating cloud with no intrinsic outward motion would have a radial velocity that is the same as that portion of the stellar disc that it occults.

The results of the simulation are presented in Figure 13*a*, which assumes a square, slablike cloudlet having a fractional area of $0.05A_\star$, a temperature of 18,000 K, a number density of 3×10^{11} cm^{-3}, a column density of 5×10^{22} cm^{-2}, and a turbulence of 10 km s^{-1}. The star is assumed to have a rotational velocity of 230 km s^{-1}. In Figure 13 we have subtracted a reference spectrum from each of the simulations, so the result is equivalent to spectrum differencing depicted in the Figure 1 gray scale. A comparison of Figure 13 with Figure 1 between times 0 and 500 minutes shows certain similarities. The narrow, blue-to-red drifting features from the S IV lines are pronounced. The Si V core is a broad, almost stationary, feature with a width of $\sim$1.5 Å. As the cloud begins to occult the star, the absorption strengthens, reaches a maximum as the cloud passes disc center and then weakens. One of the primary discrepancies between the two figures is the light colored band in Figure 13*a*, which is predicted to drift through the broad Si IV feature at a similar rate to that of the narrow S IV features. The center of this band is located at the radial velocity of the absorbing cloud.

To understand why this drifting feature does not appear in the observations, we note that the rapid variability of the MSFs as seen in the S IV lines suggests a highly dynamic structure in which condensations rapidly appear and disappear. Such a behavior implies the existence of a wide range of densities within the source region. While some parts of the structure might not be visible in the S IV and other warm plasma lines, it is likely that they are still very optically thick in Si IV. To investigate the effect of these less opaque regions we ran a second CIRCUS simulation in which we considered two adjacent (but not overlapping) cloudlets. The first cloudlet is identical to that used in our first simulation. The second has the same temperature and turbulence as the first but is smaller and less opaque, having a column mass of only 5×10^{21} cm^{-2}. Thus, it is moderately optically thick in the Si IV lines but optically thin in the S IV lines. The Si IV absorption profile for this cloud is saturated in the core and has a rectangular shape, since the cloud is not optically deep enough to form the pressure broadened wings. Projecting this cloud against the stellar surface results in a rectangular absorption feature, centered at the radial velocity of the cloud and having a width approximately three times the turbulent Doppler width and a depth that is determined almost exclusively by the projected size. This additional absorption acts to fill in the core of the profile caused by the first cloud and therefore masks the drifting feature, as seen in Figure 13*b*. Thus, the effect of many different lines of

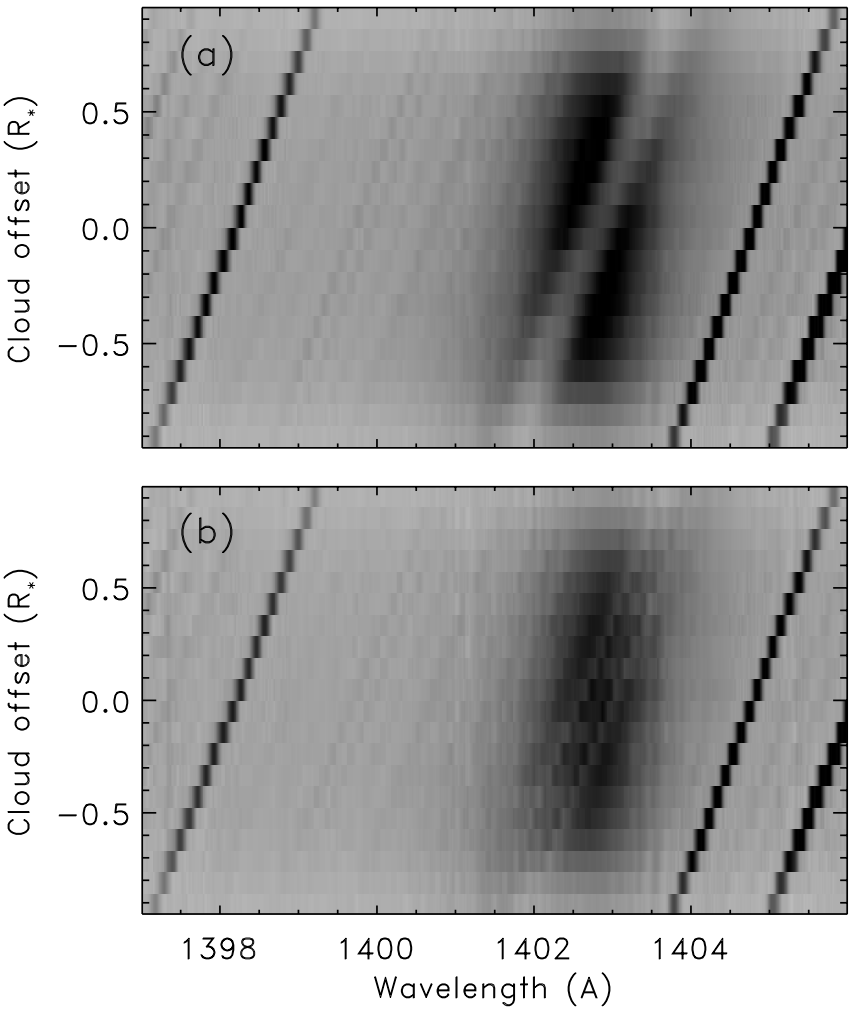

FIG. 13.—(*a*) Simulations of differential absorptions caused by a corotating occulting cloud that is highly optically thick in the Si IV lines (see text). The diagonal features to the left and right of the figure are weak absorptions from S IV exhibiting redward migration across the spectrum. The same trend is apparent in the light colored feature that drifts through the core of the broad Si IV profile. (*b*) Simulations similar to those in the top panel but with a smaller second cloud that is only mildly optically thick in the Si IV lines added. The effect of this second cloud is to remove flux preferentially in the line core and suppress the appearance of redward drift of the dark feature through the core of the profile.

sight passing through dense and rarefied regions of the corotating cloudlet can naturally explain the absence of wavelength drifts in the Si IV line profile that are so apparent in weaker lines.

4.2. *The Ultrasharp Features*: *Blob Ejections*

Although the USFs were the easiest to identify in our spectra, their interpretation is not straightforward. The fact that the USFs appear at large redshifts as well as blueshifts[6] rules out any association of the USFs with wind-induced phenomena. Likewise, the size of the positive velocities precludes explanations that invoke infalling matter. Unlike most of the profile of the wind features, the USFs are optically thick (see § 3.1.1). This fact means that the measured velocity is likely the true velocity along the line of sight of these structures. With velocities of 1000–1700 km s^{-1}, these blobs could traverse 1–5$R_\star$ in their visible lifetimes. Such distances and the absence of clear redward accelerations during their lifetimes firmly rule out models in which the parcels are part of flows rooted to surface structures.

The most likely explanation for the USFs is that they arise from blobs that are ejected from an unstable site and maintain a constant velocity. A possible explanation for the blueshifted features might be that they result from mass transients occurring near γ Cas similar to the coronal mass ejections (CME) events observed in the solar corona. These events are caused by the relaxations of stresses of large-scale magnetic loop arcades, often in association with a solar flare and the ensuing ejections of matter. Flare-related CMEs are known to maintain nearly constant velocities throughout most of their lifetimes (see, e.g., Wagner 1984). However, such events cannot explain the redshifted USFs in our data, which often have velocities considerably larger than the free-fall velocity at the surface of γ Cas (∼800 km s^{-1}; see Fig. 7).

For the last 50 years or so, γ Cas has had an active circumstellar disk. One might consider whether the circumstellar disc is somehow responsible for the ejection of small structures. The problem with this idea is that optical interferometry places the disc at an inclination of 45° to our line of sight. With this orientation it becomes difficult to under-

[6] The blueshifted USFs are harder to observe because of interference by the DACs. However, we suspect they are present at negative velocities greater than the terminal wind limit.

stand how matter from the disc could become visible along our line of sight. Accordingly, we present a highly schematic picture in which magnetic fields become an essential ingredient in the plasmoid ejection process. In this scenario magnetic fields from the star would interact with fields generated by a hydrodynamic dynamo within the dense, equatorial disc (Hawley, Gammie, & Balbus 1996 discuss such a disc). Alternatively, the disc may be nonmagnetic but be diffusive enough to allow the stellar field lines to thread longitudinally within it. Whether it is intrinsically magnetic or not, the disc is likely to have a Keplerian angular velocity that is smaller than the angular rotational velocity of the star. Magnetic fields connecting the star and disc will therefore by subjected to substantial stresses, which would ultimately lead to magnetic instabilities, as depicted in Figure 14, with a subsequent reconnection, relaxation of the field lines, and ejection of ambient material.

While instabilities can presumably occur anywhere within the loop-loop system, we note that ejections of substantial mass can take place only where the density of matter is high. We would therefore expect these sites to be either near the star or near the disc. Instabilities near the star (see Fig. 14, *upper panel*) would result in ejections both outward and inward toward the star. Inwardly directed matter would impact the star and produce X-rays, either as the primary or a secondary source of the soft X-rays we observe. Such flows could be associated with the short-lived, USF-like features observed early in our time series. The outward-directed ejections, on the other hand, would have much longer lifetimes. Instabilities within the disc would result in a preferential ejection of disc material toward the star and away from the equatorial plane, as suggested in the lower panel of Figure 14. These instabilities supply energy and direction to the flow, rather than a simple transfer of angular momentum between the magnetic fields and disc inhomogeneities (see, e.g., Ultchin, Regev, & Bertout 1997), which would eject the mass away from the star. Instabilities near the star could conceivably be related to flares and would therefore be strongly correlated with a maximum in the X-ray light curve and a minimum in the

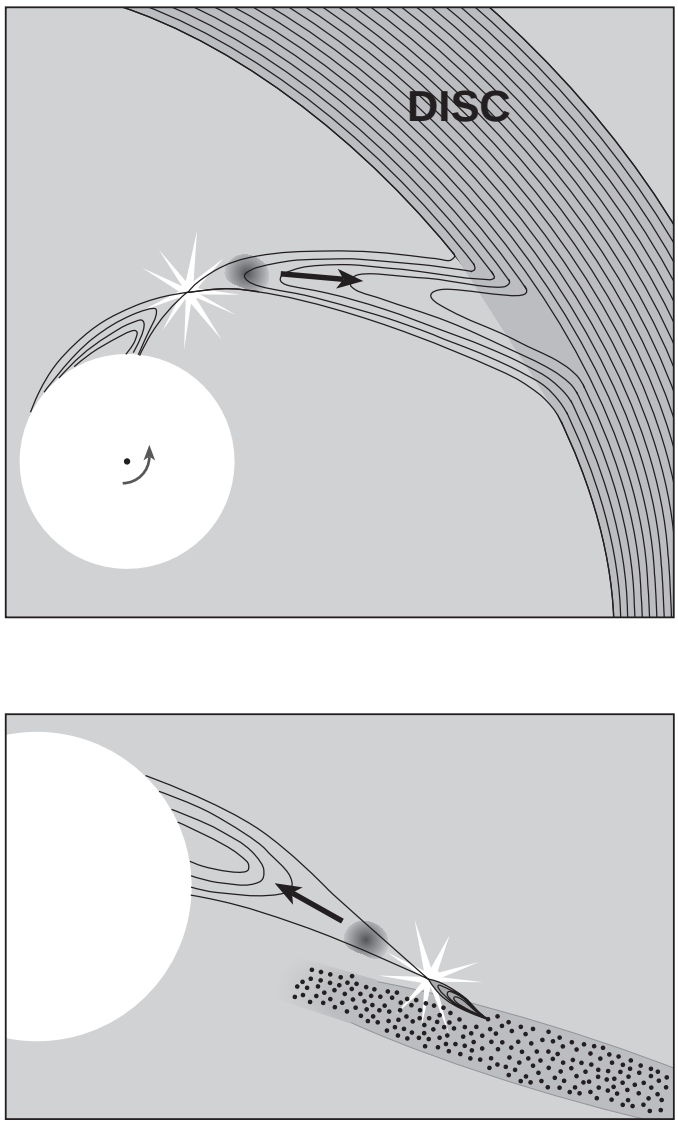

FIG. 14.—Artist's depiction of the envisioned interaction between magnetic loop systems from γ Cas and its CS disc as seen from (*upper panel*) above the star's pole and (*lower panel*) within the plane of the disc. The depictions portray two different entanglements of loop systems from fields of (*upper panel*) the star and (*lower panel*) the disc. The tangling loops create an X-point, reconnect, and relax, causing the expulsion of material (CMEs).

UVC curve. Note that blobs ejected from the disc become visible only after they start to occult the stellar surface, sometime after their ejection from the disc. This would account for their rapid onset and lack of acceleration.

A surprising feature of the USFs is the high temperatures implied by the presence of Fe V in many of the systems (see, e.g., § 3.2.2). These lines probably arise in a plasma with an ionization temperature of 34,000 $\pm$ 3000 K, so one would ordinarily expect to see them in emission, not absorption, against a star with an effective temperature of $\sim$28,000 K. Their appearance in absorption thus implies that the distribution of atomic levels, and hence excitation temperature, is much lower than their ionization temperature. This difference could be due to the stellar radiation field being diluted by distance or to some aspect of the atoms being in a highly nonthermal state. Either alternative would be consistent with their formation from an explosive event, as proposed above.

5. SUMMARY AND CONCLUSIONS

In Paper II of this series we identified the existence of at least two absorbing clouds that are located near the site of strong X-ray enhancements. These clouds produce a variation in the UV continuum and have a color that is consistent with absorption within the very extended wings of Lyα. This led us to the conclusion that hydrogen must be partially recombined in the clouds and that the cloud temperature must be $<$10,000 K. In the present study we found evidence for the presence of the Fe II 1413 Å line with a strength that varies approximately in phase with UV continuum, confirming the cool temperature of these clouds. This conclusion was further strengthened by the discovery of Fe II in our time series and by the discovery of other cool-plasma lines in an archival GHRS spectrum at a time consistent with the phase at which the larger cloud occults the star.

In the present paper we also find evidence for several other clouds or cloud complexes, which we have referred to as cloudlets to differentiate them from the cool clouds found in Paper II. The first three of these cloudlets have temperatures of $\sim$18,000 K, a temperature consistent with radiative equilibrium processes at the top of the atmosphere. These three cloudlets reach the stellar meridian in our line of sight at times $\sim$250, 800, and 1150 minutes in our observations. These cloudlets produce variations near the core of the photospheric Si IV resonance line profiles. They appear to lead the cool clouds by 100–200 minutes. Each is moderately massive, having a particle density of $>2 \times 10^{11}$ cm^{-3}, a column density of $\sim 10^{23}$ cm^{-2}, and a mass of $\sim 10^{-12}$ $M_{\odot}$. These structures are primarily responsible for numerous drifting features (the MSFs) that arise from S IV and other warm lines. The rate of drift for these features allowed us to estimate an average height for the cloudlets of $\sim 1.5R_{\star}$ above the star. There is no evidence for drifting features within the core of the Si IV line profile. This was quite puzzling until we realized that these drifts could be masked when the cloudlet was composed of at least two components, one having optical depth large enough that pressure-broadened wings appear and a second, presumably smaller, component having a lower optical depth where the wings are absent.

An examination of the Si IV profiles shows that the centroid is blueshifted by about 30 km s^{-1}, suggesting a systemic outward motion. A much larger blueshift ($-$170 km s^{-1}) was found in the fourth and fifth cloudlets discovered. These "tepid" cloudlets appear to have a cooler temperature than the other two cloudlets, since it appears in Si III and Ni II lines as well as S IV. The time history of these features (which peak in absorption near times 150 and 800 minutes) does not match that of either of the warm Si IV absorbing cloudlets or the cool clouds, so they are likely offset from both groups.

In addition to confined structures that are tied to the surface of the star, the data also suggest the existence of transient blobs of material that are not tied to the surface. These move at a relatively constant velocity and are extremely narrow, prompting the designation "ultra sharp features" ("USFs"). Blueshifted features are easily explained as ejections from the stellar surface.[7] The many redshifted features are more difficult to model. Some features have velocities well in excess of the terminal infall velocity (800 km s^{-1}) and thus cannot be associated with gravitational infall. The relatively long lifetimes and high velocities of these features suggest that they are formed at some distance from the star. The only picture we have been able to suggest that conforms to these properties is one in which highly dynamic magnetic fields connect the star to it equatorial disc. In this scenario the blobs are ejected from the stellar disc as the result of magnetic instabilities, which accelerate the plasma and direct it toward the stellar surface.

Although this star-disc interaction paradigm may seem ad hoc at first, it has several attractive properties that could not be matched by a variety of other pictures we first envisaged and eventually discarded. First, the high temperature associated with the X-rays from γ Cas may not be attainable simply from dissipation of stellar magnetic loop energy alone. The "help" from the entanglement of fields generated in a disc that orbits the star at a different angular velocity may be just what is required to produce the stresses that cause the high-temperature, flaring X-ray characteristics that are so peculiar for an upper main-sequence star. Second, the apparent absence of acceleration in the USFs, so difficult to explain by other mechanisms, gains plausibility if ejections occur far from the star where the gravitational potential well is shallow. More importantly, the disc-star magnetic-interaction scenario holds the promise of placing the hot, flaring X-rays of γ Cas into a more general context of stellar physics. In Paper I we remarked that this star's unique X-ray characteristics, whether caused by surface flares or activity associated with a postulated companion, make it the "odd man out" among X-ray emitters. The loop interaction picture predicts that other Be stars with Bp-type surface magnetic centers could show similar X-ray properties if they develop dense circumstellar discs. Thus, γ Cas may be the first member of a new class of X-ray stars.

The picture we describe apparently has not yet been treated theoretically. In fact, only recently has the stability of accretion discs embedded in a poloidal field been followed hydrodynamically (see, e.g., Hawley & Balbus 1991; Lubow & Spruit 1995). One might ask whether other types of stars in the HR diagram exhibit X-ray flaring that could be brought about by magnetic stresses from asynchronous star-disc interactions. We have surveyed the recent literature to find three general classes of X-ray emitting stars in

[7] Note that they are too dense to be explained as wind inhomogeneities.

which loop interactions could conceivably be important: cataclysmic variables, T Tauri stars, and RS CVn systems. Among cataclysmic variables, X-ray flare temperatures often attain $\sim 10^8$ K (e.g., in DQ Her stars), but such temperatures probably result from the thermalization of gravitational energy in a steep potential well (see, e.g., Patterson 1994) and can probably be dismissed in the present context. The RS CVn stars provide an attractive possibility for loop-loop interactions (see, e.g., the loop interaction picture of Simon, Linsky, & Schiffer 1980), but this applies to loops of component stars that interact in a close binary system. Observations of inverse P Cygni profiles in some T Tauri star spectra have led to a consensus that these stars accrete hot matter from the protostellar environment, which is first heated by a hot magnetosphere (see, e.g., Edwards 1997). Shu and collaborators (see, e.g., Shu et al. 1994) have introduced the concept of an "X-wind," in which infalling matter is diverted and expelled by centrifugal forces into a high-velocity wind (jets) at high latitudes. In such pictures the lines of force from the stellar field can become threaded through a disk of imperfect conductivity (see, e.g., Van Balegooijen 1994), leading to their entanglement, reconnection, and the excitation of hypothesized flares. A similar process has been invoked to explain the heating of the putative magnetospheric gas (Hartmann 1997). It is interesting that the wind flux from γ Cas is similar to the accretion rates of these T Tauri stars (Hartmannn 1997), making the flux rates for these "engines" comparable. However, given the relative faintness of T Tauri stars, it is doubtful that the ultrasharp features we believe could be related to CMEs will be observed in these stars' spectra any time soon. For the near future, it may be fruitful to search for magnetic fields on the surface of γ Cas with newly constructed Zeeman analyzers.

We wish to thank D. Meyer and M. Jura for sending us their reduced GHRS spectrum of the 1356 Å region of γ Cas. We also acknowledge I. Hubeny for providing us with his SYNSPEC and CIRCUS software, without which key quantitative aspects of this study would not have been possible. This paper has profited from many conversations with J. Patterson, E. Sion, P. Szkody, and R. Wade. These have very much improved the quality of our conclusions. We thank finally the referee of this paper, Alex Fullerton, whose comments improved the clarity of several points in the text and the figures. This study was supported in part by NASA contract GO-6086.01-94A.

REFERENCES

Balona, L. A. 1999, MNRAS, in press
Cameron-Collier, A., & Robinson, R. D. 1989, MNRAS, 236, 57
Doazan, V. 1982, in The B Stars with and without Emission, ed. A. Underhill & V. Doazan, NASA SP-456 (Washington, DC: NASA), 326
Doazan, V., Rusconi, L., Sedmak, G., Thomas, R. N., & Bourdonneau, B. 1987, A&A, 182, L25
Edwards, S. 1997, Herbig-Haro Flows and the Birth of Low Mass Stars, ed. B. Reipurth & C. Bertout (Dordrecht: Kluwer), 433
Fullerton, A. W., Gies, D. R., & Bolton, C. T. 1991, ApJS, 103, 475
Hartmann, L. 1997, Herbig-Haro Flows and the Birth of Low Mass Stars, ed. B. Reipurth & C. Bertout (Dordrecht: Kluwer), 391
Hawley, J. F., & Balbus, S. A. 1991, ApJ, 376, 223
Hawley, J. F., Gammie, C. F., & Balbus, S. A. 1996, ApJ, 464, 690
Horaguchi, T., et al. 1994, PASJ, 46, 9
Hubeny, I., & Heap, S. R. 1996, ApJ, 470, 1144
Hubeny, I., Heap, S. R., & Lanz, T. 1997, in ASP Conf. Ser. 131, Boulder-Munich Workshop II: Properties of Hot, Luminous Stars, ed. I Howarth (San Francisco: ASP), 108
Hubeny, I., Lanz, T., & Jeffery, S. 1994, Newsl. Anal. Astron. Spectra, 20, 30
Jernigan, J. G. 1976, IAU Circ. 2900
Kubo, S., Murakami, T., & Ishida, M. 1999, PASJ, in press
Kurucz, R. L. 1993, ATLAS9 Stellar Atmospheres and 2 km s^{-1} Grids, Kurucz CD-ROM 13 (Cambridge: Smithsonian Astrophys. Obs.)
Lubow, S. H., & Spruit, H. C. 1995, ApJ, 445, 337
Mason, K. O., White, N. E., & Sanford, P. W. 1976, Nature, 260, 690
Meyer, D. M., Jura, M., & Cardelli, J. A. 1998, ApJ, 493, 222
Mourard, D., Bosc, I., & Labayerie, A. 1989, Nature, 343, 520
Murakami, T., Koyama, K., Inoue, H., & Agrawal, P. C. 1986, ApJ, 310, L31
Papaloizou, J. C., Savonije, G. J., & Henrichs, H. F. 1992, A&A, 265, L45
Patterson, J. 1994, PASP, 106, 209
Quirrenbach, A., et al. 1997, ApJ, 479, 477
Serio, S., Peres, G., Vaiana, G. S., Golub, L., & Rosner, R. 1981, ApJ, 243, 288
Shu, F., Najita, J., Ostriker, E., Wilkin, F., Ruden, S., & Lizano, S. 1994, ApJ, 429, 781
Simon, T., Linsky, J. L., & Schiffer, F. H. 1980, ApJ, 239, 911
Slettebak, A. 1982, ApJS, 50, 55
Smith, M. A. 1995, ApJ, 442, 812
Smith, M. A., Robinson, R. D., & Corbet, R. H. D. 1998a, ApJ, 503, 877 (Paper I)
Smith, M. A., Robinson, R. D., & Hatzes, A. P. 1998b, ApJ, 507, 945 (Paper II)
Stee, Ph., Vakili, F., Bonneau, D., & Mourard, D. 1998, A&A, 332, 268
Stee, Ph., et al. 1995, A&A, 300, 219
Telting, J. H., & Kaper, L. 1994, A&A, 284, 515
Ultchin, Y., Regev, O., & Bertout, C. 1997, ApJ, 486, 397
Van Ballegooijen, A. 1994, Space Sci. Rev., 68, 299
Wagner, W. J. 1984, ARA&A, 22, 267
Waters, L. B., van der Veen, W. F., Taylor, A. R., Marlborough, J. M., & Dougherty, S. M. 1991, A&A, 244, 120
Yang, S., Ninkov, Z., & Walker, G. A. H. 1988, PASP, 100, 233